Assessment of Uav-Based Photogrammetry in Lahar Valleys to Estimate Boulder Potential Hazards – Field Experiment at Unzen Volcano (Japan)

Miki Sakamoto, Christopher Gome

Abstract: ***On volcanoes where lahars are triggered, the size of sediments and clasts is an important element to consider for hazards and risks. However, sediment analysed are mostly the fine fractions due to logistics issues. Recent advances in 3D capture technologies such as the terrestrial laser scanner (TLS) provide high precision topographical data that can be used to assess the largest clasts sizes, but instruments are still costly and are difficult to carry in the field due to their heavy weight. For this reason, the present contribution investigates the use of structure from motion (SfM) to assess the potential hazards due to large clasts transported by lahars. We used the SfM method from aerial photographs taken by UAV combined with ground control points, in order to obtain Orthophotos and DEMs to measure the size of boulders in the Gokurakudani gully, at Unzen volcano. Furthermore, the results are used for calculation of the prediction of behaviour of each boulder. Specifically, the critical shear stress and the physical energy of each boulder are calculated, showing that the shear stress range needed to transport such boulder range between 500 and 1200 Pascals, depending on their orientation in the valley and their size.***

Keywords: UAV; Structure from Motion; Lahar; Geomorphology; Unzen Volcano

I. INTRODUCTION

Lahars are mixtures of debris and water flowing on or from the slope of a volcano (Smith and Fritz, 1989), which contribute to the sediment cascade, eroding volcanoes, and presenting important hazards at the foot of the latter, even in the aftermath of eruption when other processes have become quiescent. Each lahar event can include debris-flow phases (sediment concentration > 60% by volume), hyperconcentrated-flow phases (sediment concentration 20 to 60% by volume), as well as lower concentration diluted phases (Beverage and Cultberson, 1964, Smith and Lowe, 1991). Rainfall is the main trigger of lahars, when thresholds of duration/volume and intensity are reached (e.g. at Unzen (Iwamoto, 1996), at Mayon (Rodolfo and Arguden, 1991), at Pinatubo Volcano (Tungol and Regalado, 1997), at Merapi Volcano and Sakurajima (Lavigne et al., 2000) and Kelut Volcano (Dibyosaputro et al., 2015; Fakhrzad et al, 2015). Other processes can also start lahar flowage, such as lake outbursts (Procter et al., 2010a), as well as snow contributions (Cronin et al., 1996).

Despite an abundant body of literature on the subject, the details on how lahar flows and how they vary locally is at best poorly understood (Starheim et al., 2013) and deviations from existing concepts and models even include the relation between sedimentary deposits and the processes that emplaced them (Gomez and Lavigne, 2010, Gomez et al., 2018; Parvizian et al, 2015; İnci & Esmer, 2018). One of these difficulties arise from the lack of integration of boulders and all the oversized clasts in sediment sampling and in the flow models, like LaharZ (Munoz-Salinas et al., 2009) and Titan 2D (Procter et al., 2010b). One of the central question to better understand the role of blocks in lahar flowage and lahar hazards is to map and measure where those blocks are located, and their sizes in 3D. Contributing to this growing body of literature, the present research aims to calculate the energy necessary for starting large boulders' movement and at the other end, to estimate the potential energy at impact of those boulders. For this purpose, the present contribution presents the results of a UAV-based photogrammetric investigation, to (1) test the feasibility of UAV (Unmanned Aerial Vehicle) photogrammetry to complete grain-size datasets, and (2) provide measures of the boulders and oversized clasts-related hazards at Unzen Volcano, preceding the potential reopening of the areas the Ministry of Land, Transport, Infrastructure and Tourism had cordoned off after the 1990-1995 eruption.

In recent years, the plunging costs of personal UAVs combined with easily operable photogrammetric methods have seen an explosion of aerial applications in Disaster Risk Management (Gomez and Purdie, 2016) and Earth Sciences – from the coast: e.g. coastline movement (Goncalves & Henriques, 2015), small elevation change on mudflats, cliff retreat (Barlow et al., 2017), to the mountains and volcanoes: , including human constructs (e.g. building impacted after L'Aquila earthquake (Dominici et al., 2017) - eventually providing dataset not acquirable before such as moving objects and gas volumes (Gomez and Kennedy, 2018). It also allows the repeat of surveys at a high frequency for geospatial data collection in countries where acquisition can be difficult (Sari and Kushardono, 2015), and in environments where the changes are very rapid, such as glacier melting (Purdie et al., 2016).

For this research, we collected data from Unzen Volcano (1359 m a.s.l.), a stratovolcano located on Shimabara peninsula, Kyushu Island, in South Japan (Fig. 1). It is a back-arc volcano that emerges above sea level 16 km N-S and 15 km EW (Yamamoto et al., 1993) for a total volume of 100 km^3

Revised Manuscript Received on April 12, 2019.

Miki Sakamoto, researchers in VoRAS Laboratory, Kobe University, Graduate School of Maritime Science, Japan

Christopher Gomez, Associate Professor and head of VoRAS Laboratory, Kobe University, Graduate School of Maritime Science, Japan.

mostly composed of andesite and dacite, emplaced above older Pliocene formations composed of basaltic andesite lava, siltstones and sandstones (Otsuka and Furukawa, 1988). Most of those formations are invisible, because the volcano is located in its "own" graben, like several of its counterparts (e.g. Merapi Volcano).

Unzen Volcano last erupted in 1990-1995, producing series of block-and-ash flow pyroclastic flows that mantled the slopes of the volcano, with a concentration of the activity towards the East, around the main axis of the Mizunashigawa River.

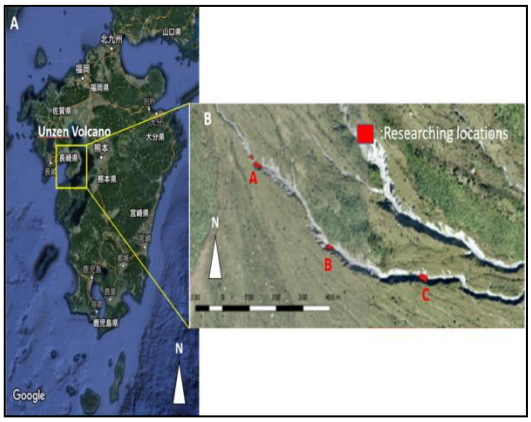

Figure. 1 Location map of Unzen Volcano and the location area. (A) Kyushu island and location of Unzen Volcano on Shimabara Peninsula; (B) Survey locations in the Gokurakudani gully on the Eastern flank of Unzen Volcano. Source: Sakamoto and Gomez, 2019.

II. RESEARCH METHOD

At three locations (location A (130.306541850°E, 32.752552659°N), B (130.309765468°E, 32.750398596°N), and location C (130.31332638°E, 32.74971104°N)) in the Gokurakudani, the authors flew the DJI Phantom-4 Pro UAV at 30 m and 50 m above ground level, collecting aerial photographs for photogrammetric purposes. At location A 543 photographs were taken, at location B, 147 photographs and at location C, 172 photographs. At the three locations, boulders marking and numbering was performed to constrain the photogrammetric data, and to compare field measurements of the boulders with the calculations from SfM. We chose boulders that were not partially buried in the sediments to limit the related error. The photogrammetric method is based on the Structure from Motion (SfM), which was performed using the software Agisoft PhotoscanPro on a classic desktop computer Intel Core i5 7-Gen 3.4 Ghz, with 4Gb ram and without a GPU. The process took between 8 hours and 2 weeks to produce the 3D dataset. At location A, the pointcloud was 28559472 pts, at location B, the pointcloud was 8395920 pts, and at location C, the pointcloud was 10651982 pts. The RMSE (Root Mean Square Error) was comprised between 1.2 and 1.9 m total (Tab. 1).

Table 1: RMSE from the SfM calculation at the three locations.

	Location A [m]	Location B [m]	Location C [m]
X	1.113349	0.869037	0.505569
Y	0.937015	1.360863	1.073931
Z	1.228148	0.439554	0.434589
Total	1.904177	1.643075	1.264039

Source: Sakamoto and Gomez 2019

Using the dataset generated from SfM, we first delineated the valley area using the vegetation as the outside limit, and within this polygon, we defined the centreline as being the line that was crossing the centre of the downsteam and upstream cross-sections. Because the gully reach is very short (from 15.092 to 22.959 m), there were no need to subdivide the reaches. After obtaining the gully floor longitudinal angle, we used that angle to correct for the orientations of the different boulders mapped in the valley. For each boulder, we measured the long axis along the valley main axis (Direction α) and the secondary axis (Direction β) as perpendicular. (Fig.2). Both axis cross the blocks in their centre. Angles are calculated by using the length between edge-points in 2-directions (α, β).

From those axis, we extracted the maximum thickness of the boulders following the method depicted in Fig. 3. Using the thickness measured from SfM data, and taking into account the typically oblong shape of the blocks, the volume was calculated by integration, where the distance "c to - c" (Fig. 3) is equal to 2 times the measured T (Fig. 2). From field inference and assessment of the main axis of each rock, the integrated shape was defined as a semi-ellipsoid. We assume that the volumes of the samples are close to the volumes of semi-ellipsoids, a characteristic shape used in sedimentology to estimate the morphology of grains.

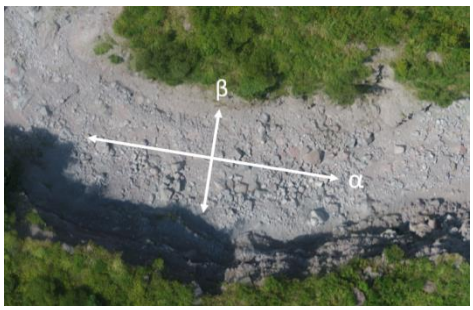

Figure. 2 Orientation of the lines along the gully direction, with α being parallel and β perpendicular to α.
Source: Sakamoto and Gomez 2019

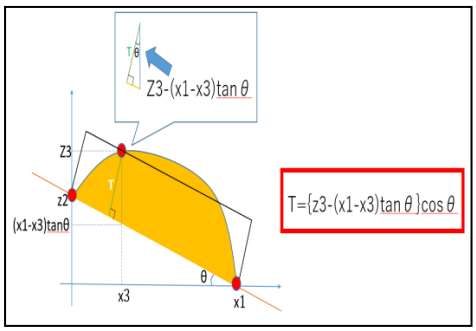

Figure. 3 Cross-section view of a hypothetical block. T in above Figure shows A thickness of a boulder.
Source: Sakamoto and Gomez 2019

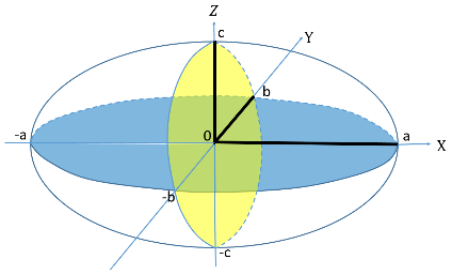

Figure. 4 Explanation of the variables used to integrate the ellipsoid: the lengths a, b and c are respectively on the x, y and z axis.

Source: Sakamoto and Gomez 2019

The equation used to calculate the ellipsoid are as follow, where equation (1) is ellipsoid shown in Fig.3, equation (2) is translation for (3), (3) is the ellipse perpendicular to x-axis in Fig.3, (4) is permutation, (5) is square root of (4);

$$\frac{x^2}{a^2}+\frac{y^2}{b^2}+\frac{z^2}{c^2}=1 \quad (1)$$

$$\frac{y^2}{b^2}+\frac{z^2}{c^2}=1-\frac{x^2}{a^2} \quad (2)$$

$$\frac{y^2}{(1-\frac{x^2}{a^2})b^2}+\frac{z^2}{(1-\frac{x^2}{a^2})c^2}=1 \quad (3)$$

$$\boldsymbol{A^2}=(1-\frac{x^2}{a^2})\,\boldsymbol{b^2}\ ,\ \boldsymbol{B^2}=(1-\frac{x^2}{a^2})\,\boldsymbol{c^2} \quad (4)$$

$$|\boldsymbol{A}|=\pm\sqrt{\boldsymbol{1}-\frac{x^2}{a^2}}\,b\ ,\ |\boldsymbol{B}|=\pm\sqrt{\boldsymbol{1}-\frac{x^2}{a^2}}\,c \quad (5)$$

Given the area of an ellipse perpendicular to x-axis as π|A||B|, then the surface perpendicular to x-axis is shown by the equation (6):

$$S(x)=\boldsymbol{\pi}\sqrt{\boldsymbol{1}-\frac{x^2}{a^2}}\,b\times\sqrt{\boldsymbol{1}-\frac{x^2}{a^2}}\,c=\pi bc(1-\frac{x^2}{a^2}) \quad (6)$$

The volume of the ellipsoid can then be calculated by integration (eq. 7);

$$\int_{-a}^{a}\boldsymbol{S(x)}\,\boldsymbol{dx}=\int_{-a}^{a}\boldsymbol{\pi bc}\left(\boldsymbol{1}-\frac{x^2}{a^2}\right)\boldsymbol{dx}=\boldsymbol{2\pi bc}\int_{0}^{a}(\boldsymbol{1}-\frac{x^2}{a^2})\,\boldsymbol{dx}=\frac{\boldsymbol{4\pi abc}}{\boldsymbol{3}} \quad (7)$$

and the volume of the semi-ellipsoid is $\frac{2\pi abc}{3}$, which is equivalent to the volume of an ellipsoid of radius is $\frac{c}{2}$ in z-axis. Combining the volume of the ellipsoids and the typical given andesite and dacite density of 2.7 g/cm3, we estimated the mass of each boulder in the gully section, for disaster risk purposes (i.e. impact potentials during remobilization).

III. RESULTS AND DISCUSSION

3.1. Results

At the three survey locations, the boulders present α-axis between 0.360m and 1.654m, and corresponding β-axis of 0.348 and 1.976m in length. The average lengths are 0.808417 and 0.797283 for the α and β axis. In α axis, maximum value is 1.654m and minimum value is 0.36m. In β axis, maximum and minimum values are 1.976m and 0.348m. The standard deviation is 0.300175 in α direction and 0.304427 in β direction. The corresponding visible surface areas from UAV photogrammetry vary between 0.146 and 2.255 m^2.(Fig. 5)

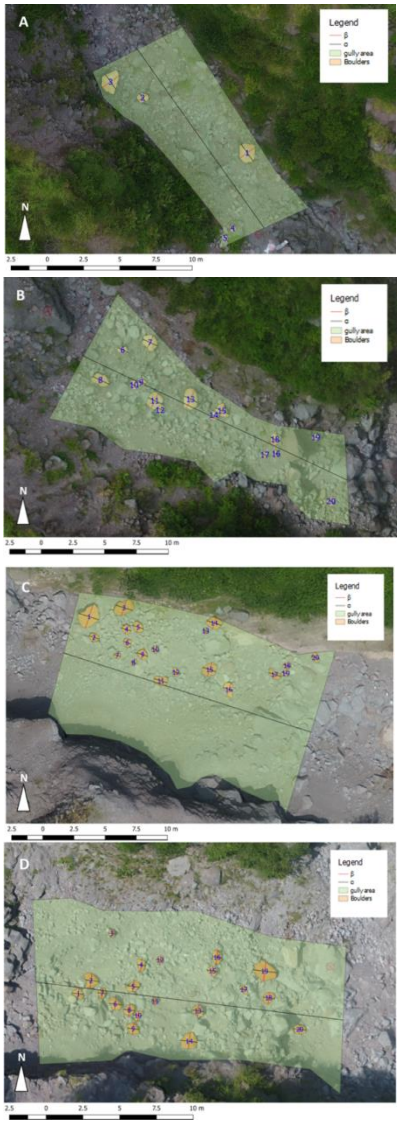

Figure. 5 Studied blocks at the three survey locations. (A) Location A upper part; (B) Location A lower part; (C) Location B; (D) Location C.

Source: Sakamoto and Gomez 2019

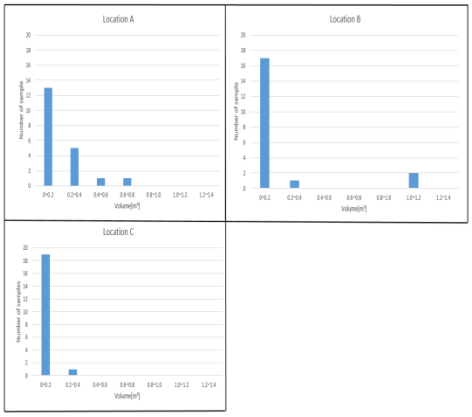

Figure. 6 Histograms of sample-volumes at location A, B, C. These values were obtained by integration (cf. Method).

Source: Sakamoto and Gomez 2019

The average calculated volume of each boulder is 0.131859m³. The maximum and minimum values are 1.140654 m³ and 0.006386 m³. At location A, the sampled boulders are dominated by samples < 0.2 m^3: 13 samples out of 20 (65 %), samples between 0.2 and 0.4 m^3 makes 25% with 5 samples and samples between 0.4 and 0.6 m³ and samples between 0.6 and 0.8 m³represents 5% each. At location B, the sampled boulders are dominated by samples < 0.2 m^3: 17 samples out of 20 blocks (85 %), samples between 0.2 and 0.4 m^3:1 sample (5%), and samples between 1.0 and 1.2 m³: 2 samples (10%). At location C, the sampled boulders are dominated by samples < 0.2 m^3: 19 samples out of 20 blocks (95 %), and samples between 0.2 and 0.4 m^3:1 sample (5%). Consequently, the mass of the samples at A are comprised between 17.24146 and 1845.647 kg, at location B, between 31.7371 and 3079.766 kg, and at location C, between 41.56185 and 799.6831 kg, samples are dominated by 78.3% of samples >80 kg.

IV. RESULTS & DISCUSSION

The results show that an important characteristic of lahar-valleys and gullies is the presence of large blocks being remobilized from pyroclastic-flow deposits and lahars, with a large variability of masses between ~17 kg and ~3000 kg, for sizes between 0.2 m^3 and 1.2 m^3. Although lahar hazards are often calculated from velocities of the fluid-phase solely, the question of how those blocks are being removed and what is their potential impact remains. We discuss these two issues using simplified physical models using (1) the critical shear stress to move a given boulder, and (2) the physical energy of a moving boulder to estimate potential impacts.

4.1. Movement initiation using critical shear stress for single boulders

One of the equations developed to calculate the critical shear stress is the Fischenish equation (8), which was first developed for river conditions, and which we assume to be comparable in the present case. Assuming that the equation holds during denser flow, we modified the fluid part from water to higher-concentration flows and provide the various results.

$$\boldsymbol{\tau_{cr} = 0.06 \times g(\rho_s - \rho_w)d \times Tan\theta} \quad (8)$$

where, g is specific gravitational acceleration. $\boldsymbol{\theta}$ is the angles of repose of the particle. $\boldsymbol{\rho_s}$ and $\boldsymbol{\rho_w}$ are the density of sediment and water. d is diameters of the samples.

Using the standard values of 9.806 m/s²as g, 2700 kg/m³ as $\boldsymbol{\rho_s}$, and 998.233 kg/m³ as $\boldsymbol{\rho_w}$. Also, the angle of repose is 42 degrees for boulders (Julien, 1995). Resulting showing slight variations suggest that depending on how a block has stopped in the valley, the results may vary. This equation is used for particles in water flow. The equation (8) shows water flow can't bring the blocks when $\boldsymbol{\rho_s}$ is larger than $\boldsymbol{\rho_w}$. We calculated critical shear stress when the samples in water flow. In Tab. 2, the results of the calculation are shown. Fig. 7 shows the histogram of the result of this calculation. In water flow, about 63% of samples can take off when the critical shear stress is less than 850 Pa. On the other hand, the histograms in Fig. 7 show that 65% of samples will be brought in less than 440Pa when the moisture in the flow is 60%. When the flow includes 40% sediments in weight, more samples can be moved by about half pressure. We supposed that if a lahar like this attacks these boulders, they will be moved by the lahar easily and the lahar can become larger and stronger. This calculation tells us the border values whether boulder move or not.

Table 2: The critical shear stress at location A, B, C. The unit is pascal [Pa].

τcr[Pa]	A	B	C
1	1268.583	1872.671	770.8876
2	597.776	781.7071	1044.981
3	1072.931	1587.758	501.3024
4	476.9585	779.9039	833.0996
5	480.565	926.8684	898.9181
6	1053.096	654.5783	866.4597
7	701.4627	550.8916	704.1675
8	1247.846	545.4819	787.1168
9	631.1361	842.1158	937.6879
10	601.3825	604.989	730.3146
11	1044.981	1049.489	477.8602
12	507.6137	692.4464	544.5803
13	1092.767	549.99	815.0672
14	599.5793	1218.994	1142.356
15	987.2771	1251.453	682.5286
16	421.0579	1246.043	913.3441
17	534.6624	1029.653	650.9718
18	669.0042	665.3977	811.4607
19	669.9059	680.7253	1572.43
20	520.2364	763.6746	803.3461

Source: Sakamoto and Gomez 2019

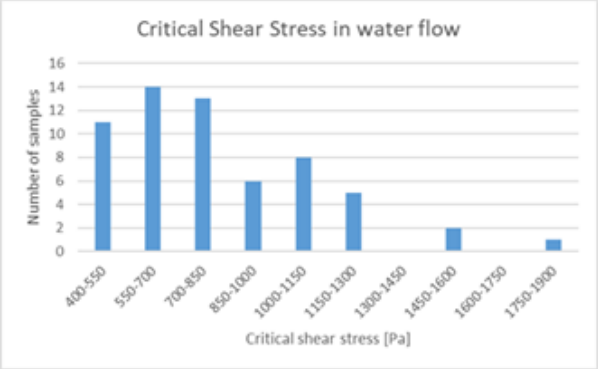

Figure. 7 The histogram of critical shear stress of 60 boulders.

Source: Sakamoto and Gomez 2019

The minimum, maximum and mean values are 421.0579Pa, 1872.671Pa and 832.7089Pa. These large values show the blocks like we chose are difficult to move. We compare the orthophotos of location C taken in June, August and November. (Fig. 8, 9, 10)

Published By:
Blue Eyes Intelligence Engineering
& Sciences Publication

Figure. 8 Location C in June, 2018.
Source: Sakamoto and Gomez 2019

Figure.9 Location C in August, 2018.
Source: Sakamoto and Gomez 2019

Figure.10 Location C in November, 2018.
Source: Sakamoto and Gomez 2019

Fig. 8, 9 and 10 tell us the alteration of the position of sediments. In particular, many blocks have been moved between June and August. We estimate the transports are caused by lahars and dropping from gully-wall. If lahars brought blocks, the pressure as large as the results of calculation is necessary without water pressure. This means the minimum of pressure of lahars happened can be guessed. Therefore, the analysis of SfM data tells us the scales of lahars. This way is suited for researching small area like we chose.

However, we don't confirm the errors this equation has.

4.2. The physical energy of moving boulders

Once the boulders are moving in lahars, they travel at the lahar speed or at a lower velocity (except on very steep slope, where a boulder can eventually reach higher velocities than the surrounding fluid mixture). Therefore, we consider:

the physical energy to be $\frac{1}{2}m\boldsymbol{v^2}$[J]. The equation of physical energy of each sample is shown the equation (12).

$$\boldsymbol{E} = \frac{1}{2}m\boldsymbol{v^2} \quad (12)$$

E is the physical energy[J], m is the mass[kg] and v means the velocity[m/s].

For using this equation, an important parameter to estimate is the velocity, and for which we have used values found in the literature *Estimation of lahar flow velocity on Popocatepetl volcano (Mexico*) (Munoz-Salinas, E. Manea, V.C. Palacios, D. Castillo-Rodriguez, M.). The values are shown in follow table (Tab. 3).

Table 3: The table of volume, distance and mean velocity.

Volume ('000 s $\boldsymbol{m^3}$)	5	25	50	100	125	1000
Distance between monitoring station and end point (m)	465	1655	2487	3128	3442	4019
Mean velocity (m/s)	2.48	4.01	4.41	4.92	5.24	11.00

Source: Sakamoto and Gomez 2019

Table 4: The physical energy of each velocity. The unit is joule [J].

id	v=2.48m/s A	B	C	id	v=4.01m/s A	B	C	id	v=4.41m/s A	B	C	id	v=4.92m/s A	B	C
1	4494.579	8623.021	513.7929	1	11750.99	22544.72	1343.302	1	14212.25	27266.74	1624.658	1	17689.51	33938	2022.158
2	236.4443	451.7303	1632.068	2	618.1791	1181.04	4267.009	2	747.6576	1428.411	5160.74	2	930.5844	1777.895	6423.401
3	1675.603	9470.895	253.1053	3	4380.831	24761.47	661.739	3	5298.402	29947.79	800.3411	3	6594.744	37275.02	996.1579
4	129.1804	753.8477	424.8039	4	337.7395	1970.92	1110.641	4	408.4795	2383.732	1343.267	4	508.4208	2966.952	1671.919
5	53.02093	1043.071	729.5474	5	138.6222	2727.087	1907.387	5	167.6568	3298.28	2306.892	5	208.6768	4105.259	2871.312
6	461.467	442.5709	1229.035	6	1206.496	1157.093	3213.288	6	1459.199	1399.448	3886.316	6	1816.216	1741.846	4837.168
7	1796.894	181.1289	403.5759	7	4697.945	473.558	1055.141	7	5681.936	572.7454	1276.142	7	7072.116	712.8771	1588.372
8	2538.887	251.2406	469.1915	8	6637.87	656.8636	1226.692	8	8028.181	794.4446	1483.624	8	9992.409	988.8187	1846.618
9	171.0488	1196.165	872.6778	9	447.2037	3127.35	2281.599	9	540.8711	3782.378	2759.483	9	673.2042	4707.8	3434.637
10	334.7333	262.717	364.0051	10	875.1536	686.8685	951.6842	10	1058.456	830.7341	1151.016	10	1317.425	1033.987	1432.631
11	2360.491	736.0963	170.6481	11	6171.457	1924.509	446.156	11	7464.077	2327.601	539.6041	11	9290.288	2897.087	671.6271
12	407.9611	324.1194	127.811	12	1066.606	847.4038	334.1593	12	1290.009	1024.894	404.1495	12	1605.63	1275.651	503.0314
13	5675.734	130.9026	784.6401	13	14839.1	342.2422	2051.426	13	17947.17	413.9253	2481.1	13	22338.24	515.199	3088.142
14	691.0215	2500.284	726.454	14	1806.662	6536.943	1899.3	14	2185.07	7906.115	2297.111	14	2719.684	9840.477	2859.137
15	2012.573	1109.626	374.261	15	5314.122	2901.095	978.498	15	6427.172	3508.734	1183.446	15	7999.687	4367.204	1472.995
16	180.7435	250.6458	588.0694	16	472.5504	655.3086	2583.288	16	571.5267	792.5639	3124.361	16	711.3602	986.4778	3888.788
17	229.4022	268.3148	240.2796	17	599.7675	701.5038	628.2062	17	725.3897	848.4347	759.7849	17	902.8683	1056.018	945.6788
18	725.5202	97.59793	556.449	18	1896.858	255.1679	1454.825	18	2294.158	308.6131	1759.54	18	2855.462	384.1205	2190.041
19	299.7453	227.7105	2459.185	19	783.6783	595.3446	6429.492	19	947.8208	720.0403	7776.158	19	1179.721	896.2101	9678.724
20	639.7005	546.4076	614.8968	20	1672.484	1428.572	1607.636	20	2022.789	1727.788	1944.357	20	2517.698	2150.52	2420.076

id	v=5.24m/s A	B	C	id	v=11.00m/s A	B	C
1	20065.42	38496.27	2293.757	1	88424.18	169645.1	10108.11
2	1055.573	2016.687	7286.138	2	4651.692	8887.124	32108.51
3	7480.495	42281.49	1129.953	3	32965	186325.8	4979.472
4	576.7076	3365.448	1896.478	4	2541.432	14830.84	8357.387
5	236.7045	4656.642	3256.962	5	1043.108	20520.87	14352.76
6	2060.155	1975.796	5486.855	6	9078.679	8706.927	24179.44
7	8021.983	808.6247	1801.708	7	35351.23	3563.443	7939.758
8	11334.5	1121.629	2094.64	8	49948.83	4942.786	9230.647
9	763.6233	5340.112	3895.948	9	3365.131	23532.77	17168.64
10	1494.37	1172.863	1625.05	10	6585.381	5168.568	7161.261
11	10538.08	3286.199	761.8345	11	46439.16	14481.6	3357.248
12	1821.285	1446.986	570.5943	12	8026.03	6376.569	2514.492
13	25338.52	584.3962	3502.916	13	111661.7	2575.314	15436.63
14	3084.969	11162.17	3243.152	14	13594.82	49189.38	14291.91
15	9074.137	4953.77	1670.836	15	39987.86	21830.25	7363.03
16	806.9041	1118.973	4411.097	16	3555.861	4931.085	19438.8
17	1024.134	1197.854	1072.694	17	4513.148	5278.696	4727.144
18	3238.984	435.7123	2484.189	18	14273.54	1920.095	10947.31
19	1338.171	1016.582	10978.69	19	5897.045	4479.866	48380.83
20	2855.853	2439.36	2745.121	20	12585.16	10749.76	12097.18

Source: Sakamoto and Gomez 2019

Table 5: The physical energy of a boulder moving at the velocity.

	2.48m/s	4.01m/s	4.41m/s	4.92m/s	5.24m/s	11.00m/s
Maximum energy [J]	9470.895	24761.47	29947.79	37275.02	42281.49	186325.8
Minimum energy [J]	53.02093	138.6222	167.6568	208.6768	236.7045	1043.108
Mean energy [J]	1132.289	2960.347	3580.396	4456.4	5054.946	22276.11

Source: Sakamoto and Gomez 2019

These values tell us the energies of boulders when they are moving as lahars. That will be useful for planning of structures such as Sabo dams and buildings. This way using SfM tells us the risk of lahars in each field at low cost. However, we must not forget these values are estimated as index of physical energy because the boulders loss energy during rolling or they get more energy by acceleration

V. CONCLUSION

This research shows one of examples of topographic surveys with SfM. We researched the sizes of boulders in Gokurakudani gully in Unzen volcano by using SfM. Using SfM enable to obtain data in area where people cannot approach at low cost. The data from SfM was used the examining the motion of boulders. In this research, we calculated the critical shear stress and the physical energy of boulders as examples of analysis. The results of these tell us the risk in the area. This way of analysis can be applied to various situations. Therefore, we consider SfM gives us the elements for predicting of hazards.

VI. ACKNOWLEDGEMENTS

Acknowledgements can be delivered to the parties who have helped research and completion of the writing of the manuscript. These parties can act as mentors, funders, providers of data, and so forth.

REFERENCES

1. Barlow, J., J. Gilham, C.I. Ibarra. 2017. “Kinematic analysis of sea cliff stability using UAV photogrammetry”. *International Journal of Remote Sensing* 38: 8-10.
2. Beverage, J.P., and J.K. Culbertson. 1964. “Hyperconcentrations of suspended-sediment”. *American Society of Civil Engineers* 90: 117-126.
3. Cronin, S.J., V.E. Neall, J.A. Lecointre, A.S. Palmer. 1996. “Unusual “snow slurry” lahars from Ruapehu volcano, New Zealand”. *Geology* 24: 1107-1110.
4. Dibyosaputro, S., G.A. Dipayana, H. Nugraha, K. Pratiwi, H.P. Valeda. 2015. “Lahar at Kali Konto after the 2014 Eruption of Kelud Volcano, East Java: Impacts and Risks”. *Forum Geografi* 29: 59-72.
5. Dominici, D., M. Alicandro, V. Massimi. 2015. “UAV photogrammetry in the post-earthquake scenario: case studies in L’Aquila”. *Geomatics, Natural Hazards and Risk* 8: 87-103.
6. Fakhrzad, M. B., Golmohammadi, A. M., & Bagheri, F. A mathematical model for P-hub median location problem to multiple assignment between non-hub to hub nodes under fuzzy environment. *UCT Journal of Research in Science, Engineering and Technology, 3*(1),39-43.
7. Gomez, C., and B. Kennedy. 2018. “Capturing volcanic plumes in 3D with UAV-based photogrammetry at Yasur Volcano – Vanuatu”. *Journal of Volcanology and Geothermal Research* 15: 84-88.
8. Gomez, C., and H. Purdie. 2016. “UAV-based Photogrammetry and Geocomputing for Hazards and Disaster Risk Monitoring - A Review”. *Geoenvironmental Disasters* 3(23): 1-11.
9. Gomez, C., F. Lavigne, D. Sri Hadmoko, P. Wassmer. 2018 “Insights into lahar deposition processes in the Curah Lengkong (Semeru Volcano, Indonesia) using photogrammetry-based geospatial analysis, near-surface geophysics and CFD modelling”. *Journal of Volcanology and Geothermal Research* 353: 102-113.
10. Gomez, C., and F. Lavigne. 2010. “Transverse architecture of lahar terraces, inferred from radargrams: preliminary results from Semeru volcano, Indonesia”. *Earth Surface Processes and Landforms* 35: 1116-1121.
11. Goncalves, J.A., and R. Henriques .2015. “UAV photogrammetry for topographic monitoring of coastal areas”. *ISPRS Journal of Photogrammetry and Remote Sensing* 104: 101-111.
12. İnci, A., & Esmer, A. Ç. (2018). Investigation of Parvovirus B19 IgG and IgM antibodies with ELISA, distribution with regard to age groups and comparison with literature. *Journal of Clinical and Experimental Investigations*, *9*(1), 30-33.
13. Iwamoto, M. 1996. “Prevention of disasters caused by debris flows at Unzen volcano, Japan”. In *Geomorphic Hazard, edited by Slaymaker, O, 95-110*pp. 17-32.
14. Lavigne, F., J.-C. Thouret, B. Voight, H. Suwa, H. Sumaryono, A. 2000. “Lahar at Merapi Volcano, Central Java: an overview”. *Journal of Volcanology and Geothermal Research* 100: 423-456.
15. Munoz-Salinas, E., M. Castillo-Rodriguez, V. Manea, M. Manea, D. Palacios. 2009 “Lahar flow simulations using LAHARZ program: Application for the Popocatepelt volcano, Mexico”. *Journal of Volcanology and Geothermal Research* 182: 13-22.
16. Otsuka, H., and H. Furukawa. 1988. “Early and Middle Pleistocene stratigraphy in Kyushu, Japan”. *Memoire of the Geological Society of Japan* 30: 155-168.
17. Parvizian, F., Ghojavand, K., & Niknejadi, F. (2015). Effectiveness of Emotional Intelligence on Emotional Alexithymia of Married Women Teachers in Yasuj City. UCT Journal of Social Sciences and Humanities Research, 3(1), 32-35.
18. Procter, J.N., S.J. Cronin, I.C.Fuller, G. Lube, V. Manville. 2010a “Quantifying the geomorphic impacts of a lake-breakout lahar, Mount Ruapehu, New Zealand”. *Geology* 38: 67-70.
19. Purdie, H., P. Bealing, E. Tidey, C. Gomez, J. Harrison. 2016. “Bathymetric evolution of Tasman Glacier terminal lake, New Zealand, as determined by remote surveying techniques”. *Global and Planetary Chmnge* 147: 1-11.
20. Rodolfo, K.S., and A.T. Arguden .1991. “Rain-lahar generation and sediment-delivery systems at Mayon volcano. Fisher”. In *Sedimentation in Volcanic Settings*, edited by V. Smith, G. 45, 71-87. *SEPM Spec. Pub.*
21. Sari, N.M., and D. Kushardono. 2015. Object Segmentation on UAV Photo Data to Support the Provision of Rural Area Spatial Information. *Forum Geografi* 29: 49-58.
22. Smith, G.A., and W.J. Fritz. 1989. “Volcanic influences on terrestrial sedimentation”. *Geology*, 17: 375-376.
23. Smith, G.A., and A. Lowe. 1991. “Lahars: volcano-hydrologic events and deposition in the debris-flow-hyperconcentrated flow continuum”. In *Sedimentation in Volcanic Settings*, edited by Fisher, R.V. & Smith, G. 45, 59-70. *SEPM Spec. Pub.*

24. Starheim, C.A., C. Gomez, T. Davies, F. Lavigne, P. Wassmer. 2013. “In-flow evolution of lahar deposits from video-imagery with implications for post-event deposit interpretation, Mount Semeru, Indonesia”. *Journal of Volcanology and Geothermal Research* 256: 96-104.
25. Tungol, N.M., and T.S. Regalado. 1997. “Rainfall, acoustic flow monitor records, and observed lahars at Sacobia River”. In *Eruptions and Lahars at Mt. Pinatubo, Philippines, edited by* Newhall, C.G. Punongbayan, 1023-1032. *Fire and Mud.*
26. Yamamoto, T., S. Takarada, S. Suto. 1993. “Pyroclastic flows from the 1991 eruption of Unzen volcano, Japan”. *Bulletin of Volcanology* 44: 166-175.
27. Munoz-Salinas, E., V.C. Manea, D. Palacios, M. Castillo-Rodriguez. 2007. “Estimation of lahar flow velocity on Popocatepetl volcano (Mexico)”. *Geomorphology*, 92: 91-99.